IOP Publishing | Institute of Physics and Engineering in Medicine Physics in Medicine & Biology

Phys. Med. Biol. **62** (2017) 6729–6745 https://doi.org/10.1088/1361-6560/aa7721

High-energy x-ray Talbot–Lau radiography of a human knee

F Horn[1], K Gelse[2], S Jabari[3], C Hauke[1], S Kaeppler[4], V Ludwig[1], P Meyer[5], T Michel[1], J Mohr[5], G Pelzer[1], J Rieger[1], C Riess[4], M Seifert[1] and G Anton[1]

[1] Erlangen Centre for Astroparticle Physics, Friedrich-Alexander-University Erlangen-Nuremberg, Erwin-Rommel-Strasse 1, 91058 Erlangen, Germany
[2] Department of Orthopaedic and Trauma Surgery, University Hospital Erlangen, Krankenhausstrasse 12, 91054 Erlangen, Germany
[3] Department of Anatomy, University Hospital Erlangen, Krankenhausstrasse 9, 91054 Erlangen, Germany
[4] Pattern Recognition Lab, Friedrich-Alexander-University Erlangen-Nuremberg, Martensstrasse 3, 91058 Erlangen, Germany
[5] Karlsruhe Institute of Technology, Institute of Microstructure Technology, Hermann-von-Helmholtz-Platz 1, 76344 Eggenstein-Leopoldshafen, Germany

E-mail: florian.horn@fau.de

Received 28 February 2017, revised 2 May 2017
Accepted for publication 5 June 2017
Published 1 August 2017

Abstract

We report on a radiographic measurement of an *ex vivo* human knee using a grating-based phase-contrast imaging setup and a medical x-ray tube at a tube voltage of 70 kV. The measurement has been carried out using a Talbot–Lau setup that is suitable to achieve a high visibility in the energy regime of medical imaging.

In a medical reading by an experienced trauma surgeon signatures of chondrocalcinosis in the medial meniscus have been identified more evidently using the dark-field image in comparison to the conventional attenuation image. The analysis has been carried out at various dose levels down to 0.14 mGy measured as air kerma, which is a dose comparable to clinically used radiographic devices. The diagnosis has been confirmed by a histological analysis of the meniscus tissue.

In the introduced high-frequency filtered phase-contrast image the anterior and posterior horn of the medial meniscus and the posterior cruciate ligament have also been visible.

Furthermore, atherosclerotic plaque is visible in both imaging modalities, attenuation and dark-field, despite the presence of overlaying bone.

This measurement, for the first time, proves the feasibility of Talbot–Lau x-ray imaging at high-energy spectra above 40 kVp and reasonable dose levels

 © 2017 Institute of Physics and Engineering in Medicine Printed in the UK

with regard to spacious and dense objects.

Keywords: x-ray imaging, Talbot–Lau imaging, phase-contrast, dark-field, chondrocalcinosis, high-energy

(Some figures may appear in colour only in the online journal)

1. Introduction

The interaction of matter with an electromagnetic wave is described by both the real and the imaginary part of the refractive index. Up to now, medical imaging in clinical practice solely employed the latter one and consequently only the absorption property of matter has been exploited to form the image. In contrast, deflection of the x-rays is based on the real part of the refractive index. Due to the small wavelength of x-rays the angle of deflection is small (typically in the order of nanoradians), therefore difficult to measure, and has not been applied to medical imaging in the clinics yet.

Regarding x-ray laboratory setups, there exists a variety of different phase sensitive methods (Fitzgerald 2000) using the radiation of snychrotron facilities (Momose *et al* 1996, Chapman *et al* 1997, Arfelli *et al* 2000, Olivo *et al* 2001, Momose *et al* 2003) or x-ray tubes (Pfeiffer *et al* 2006, Engelhardt *et al* 2007, Olivo *et al* 2007, Parham *et al* 2009), though.

In the case of grating-based phase-contrast imaging (Momose *et al* 2003) the Talbot–Lau method (Pfeiffer *et al* 2006) made phase-contrast information accessible to standard medical x-ray tubes entailing a polychromatic spectrum and a large focal spot. The combined benefit of possibly superior soft tisse contrast (Momose 2005) as well as the retrieval of complementary information via dark-field imaging (Pfeiffer *et al* 2008) opened a window to a wide field of applications in medical imaging and non-destructive testing (Revol *et al* 2012, Bayer *et al* 2013, Prade *et al* 2016).

In terms of medical applications, imaging on animals was reported with regard to lung emphysema (Hellbach *et al* 2015) at 35 kVp and neonatal lung injury (Yaroshenko *et al* 2016). As a possibly new contrast agent for the dark-field image, microbubbles were used in an *ex vivo* mouse measurement at 35 kV tube voltage (Velroyen *et al* 2015). The first *in vivo* small-animal study at 31 kVp showed the capability of resistance against object motion (Bech *et al* 2013). Regarding human material, a relatively large number of full breast mastectomy specimens has been imaged (Stampanoni *et al* 2011, Michel *et al* 2013, Scherer *et al* 2016). Typically, mammography measurements are carried out at tube voltages up to 35 kV. A fesibility study of the imaging of human joint gaps has taken place at 40 kVp for a hand (Momose *et al* 2014) and a knee (Nagashima *et al* 2014), as well.

In summary, mostly Talbot–Lau setups using low photon energy up to 40 keV have been used in recent years (Yaroshenko *et al* 2014). Thereby, the low energy regime is technically advantageous because of slighter deflections of the x-rays at higher energies and increasingly translucent gratings with higher energies.

In general, medical applications beside mammography require higher x-ray photon energy in the range of 50 to 140 keV . A significant progress to the first attempt by Donath *et al* (2009) has been reported by Willner *et al* (2013) with a measurement carried out at a synchroton facility at 82 keV. The successfull transition to a medical tube setup at 70 kVp tube voltage comprised a computed tomography measurement of an intervertebral disk surrounded by bones showing improved soft-tissue contrast in the differential phase-contrast image compared to attenuation imaging (Sarapata *et al* 2015). A potential usecase of Talbot–Lau imaging

has been reported with the application of x-ray vector radiography measuring the bone microstructure with regard to average density and anisotropy, which could prove useful in the diagnosis of osteoporosis (Schaff *et al* 2014). This measurement has been carried out using a conventional tube with a spectrum of 50 kVp .

In order to further investigate the feasibility of high-energy Talbot–Lau radiography, we introduced a setup that is capable of measuring spacious and high-absorbing objects while even increasing visibility and maintaining sufficient sensitivity (Rieger *et al* 2017). We will show the resulting images of a recent measurement of an *ex vivo* human knee at 70 kVp revealing chondrocalcinosis, which is better visible using the dark-field signal compared to the attenuation one at a dose of 0.14 mGy . The finding was confirmed by histopathology. In addition, we will present the differential phase-contrast image of soft tissue structures, such as the posterior cruciate ligament, and signatures of calcified atherosclerotic plaque. The latter one is visible in both the attenuation and dark-field image despite the presence of overlaying bone.

2. Materials and methods

2.1. Grating-based phase-contrast imaging

Grating based phase-contrast imaging provides access to both the real and imaginary part of the energy-dependent refractive index $n(E) = 1 - \delta(E) + \mathrm{i}\beta(E)$. Thereby, the complex part β entails information about the attenuation properties of an object while the real part δ causes the deflection of x-rays passing an object. A Talbot–Lau setup regularly consists of three gratings, as depicted in figure 1.

The phase grating $G1$ impinges a phase-shift at the grating bars and thus yields a downstream fringe pattern according to the Talbot effect. At the fractional Talbot distances the intensity pattern reproduces the shape of $G1$ (Momose *et al* 2003) provided sufficient spatial coherence, which is ensured by the source grating $G0$. Thereby, the broad focus of a medical x-ray tube is split into several mutual independent slit sources, each producing its own intensity pattern. The period of $G0$ is chosen such that the intensity patterns superimpose each other constructively (Pfeiffer *et al* 2006).

As the period length of the intensity pattern is below the spatial resolution of a common flatpanel detector, the fringes cannot be resolved without the help of the analyzer grating $G2$. Thereby, the period of $G2$ is chosen to match the period of the intensity pattern. With the use of $G2$ as an absorption mask, the intensity pattern can be scanned by measuring the transmitted intensity in every pixel at several positions x_m of $G2$, whereas m marks the mth position of $G2$ distributed in fractions of its period p_2. In doing so, an intensity distribution is measured in each pixel (Weitkamp *et al* 2005). The method is referred to as phase-stepping technique. A sinusoidal curve describing the intensity modulation is fitted to the data or retrieved by fast fourier transformation, which is given by

$$I(x_m) = I_0 \left(1 + V \cdot \sin\left(\frac{2\pi}{p_2} x_m + \varphi\right)\right), \tag{1}$$

whereas I_0 indicates the mean intensity, φ the phase, and the visibility V is the relative contrast of the intensity pattern.

If the x-rays pass an object that is regularly placed in between $G0$ and $G1$, the real part of its refractive index δ induces a local phase-shift to the wavefront. A gradient of the phase perpendicular to the direction of propagation causes a deflection of the x-rays. Thereby, the angle of deflection α is directly proportional to the gradient of the phase-shift induced by the object and is described by

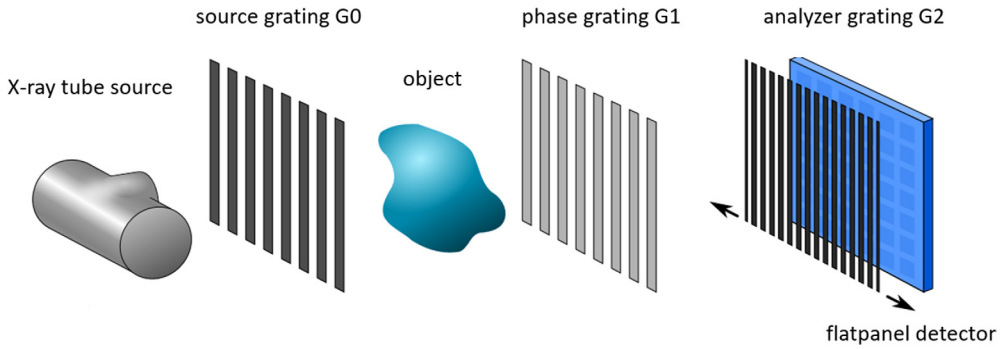

Figure 1. Sketch of the used Talbot–Lau interferometer setup. The phase grating $G1$ induces a phase-shift to the impinging wavefront at the grating bars which causes an intensity pattern downstream at certain distances. As the intensity pattern is too small to be directly resolved by a common flatpanel detector, the analyzer grating $G2$ is used to sample the fringes. Using a medical x-ray tube the source grating $G0$ is required to ensure sufficient spatial coherence.

$$\alpha = \frac{\lambda}{2\pi} \cdot \frac{\partial \Phi}{\partial x} \tag{2}$$

with λ being the wavelength (Pfeiffer *et al* 2006) and Φ being the phase. In consequence of the angular deflection the intensity fringe pattern in the Talbot distances gets shifted. Hence, the local displacement of the intensity pattern contains information about the object and can be exploited with regard to imaging.

In addition, an object with sub-pixel size microstructure causes spatial fluctuations of the wavefront (Pfeiffer *et al* 2008, Yashiro *et al* 2010, Koenig *et al* 2016), which causes a loss in the visibility of the measured phase-stepping curve. The relative reduction of the visibility can be determined to form the dark-field image and measures the unresolved micron-size substructure of the object.

Finally, the phase-stepping curve is obtained for both the reference and the object measurement. The attenuation image Γ, the differential phase-contrast image ϕ, and the dark-field image Σ can then be calculated according to

$$\Gamma = -\ln\left(\frac{I_0^{\text{obj}}}{I_0^{\text{ref}}}\right), \qquad \phi = \varphi_{\text{obj}} - \varphi_{\text{ref}}, \qquad \text{and} \qquad \Sigma = -\ln\left(\frac{V_{\text{obj}}}{V_{\text{ref}}}\right). \tag{3}$$

Thus, Talbot–Lau imaging comprises three different and complementary imaging modalities, which are retrieved from the same object and reference measurement.

2.2. Description of the used high-energy radiography setup

With its intended use for medical imaging, the Talbot–Lau setup was designed to provide high visibility in a range from 50 kVp to 125 kVp due to the requirement of low dose application, whereas visibility is crucial (Revol *et al* 2010, Chen *et al* 2011, Weber *et al* 2011). In addition, the sensitivity has to be kept at a level that is sufficient to image subtle structures of medical importance. The considerations leading to the chosen parameters are presented in a separate publication in more detail (Rieger *et al* 2017).

Table 1. Grating specifications and distances of the used Talbot–Lau interferometer.

	G0	G1	G2
Material	Au	Au	Au
Period (μm)	13.31	5.71	10.00
Height of bars (μm)	200	6.3	200
Duty cycle	0.48	0.30	0.50
Distance from source (mm)	150	1049	1724

The Talbot–Lau interferometer consists of three gratings, whose parameters are shown in table 1. The duty cyle of the phase-shifting grating $G1$ was chosen to be 0.3, as proven to be advantageous with regard to visibility in some cases recently (Rieger *et al* 2016). Thereby, the increase in visibility even comes without the possible loss in image quality due to higher absorption gratings ($G0$ and $G2$) as a straightforward option to raise visibility, which was revealed by Trimborn *et al* (2016). All gratings are made of gold at the grating bars and are fabricated by the Karlsruhe Nano Micro Facility/Karlsruhe Institute of Technology (KNMF/KIT) using deep x-ray lithography (Meyer *et al* 2015, Meyer and Schulz 2015). Thereby, the transition towards higher energies entails increasing demands with regard to the used high-aspect-ratio gratings, since the absorbing gratings become increasingly translucent with photon energy until the k-edge of gold at 80.7 keV . Hence, meeting those requirements by increasing the grating heights is essential for high-energy Talbot–Lau imaging. As a radiation source, we use a medical x-ray tube of type Siemens MEGALIX CAT Plus 125 with a tungsten anode and a focal spot size of 0.3 (IEC 60336), respectively 0.4 mm $\times$ 0.65 mm (H$\times$V) at 15% of the maximum value. The radiation is filtered with a 0.3 mm thick copper plate to suppress energies below 30 keV. For x-ray detection we use a PerkinElmer DEXELA 1512 with 74.8 μm pixel size in 2 $\times$ 2 binning mode. The distances between the tube source and the gratings are listed in table 1, as well. Thereby, it was taken care that there is enough space in front of $G1$ to place spacious specimen.

The obtained visibility averaged over the full field of view is plotted in figure 2 on the left-hand side against the tube voltage. Best visibility, namely 40%, is achieved at 50 kVp. Concerning the knee measurement using 70 kVp , it still lies at 28%. Thereby, the size of the field of view comprises an area of 20.9 mm $\times$ 22.6 mm. The local visibility over the field of view is shown on the right-hand side of figure 2 for a 70 kVp spectrum, as it was used for the measurement of the knee. The object tray can be moved to measure large specimens and the resulting images can be tiled.

2.3. Sample preparation and imaging procedure

2.3.1. Ethics statement. The measurement was conceptualized as an *ex vivo* feasibility study. The use of human tissues for this experiment was approved by the Ethics Committee of the University of Erlangen-Nuremberg (Germany). Tissues were used with the patient's or body donator's written consent.

For reasons of conservation, the knee has been stored in a formaldehyde solution. During the measurement it was taken out of the formaldehyde bath, placed in a plastic box, and retained by sponges, which are visible in the images shown below, especially in the differential phase-contrast image.

The knee was measured at 11 phase-step positions over 2 grating periods with an acquisition time of 35 ms each. The measurement was repeated fourteen times allowing to combine these images afterwards for different dose levels. Thereby, for half of the measurements the

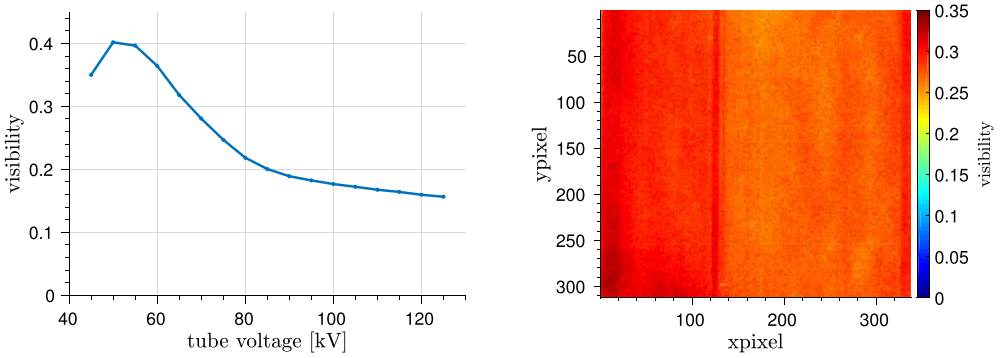

Figure 2. On the left-hand side: mean visibility over the complete G2 area of size 50.5 mm × 46.7 mm as a function of tube voltage. At 70 kV tube voltage the averaged visibility amounts to 28%. On the right-hand side: local visibility over field of view for a 70 kVp measurement without object. The highest measured visibility is 34%.

knee was rotated by 90° around an axis parallel to the direction of propagation to obtain complementary two-directional differential phase-contrast and dark-field images (Kottler *et al* 2007, Jensen *et al* 2010, Scherer *et al* 2014). The images of one orientation have been registered to the images of the other orientation using a built-in MATLAB function to reduce mismatches. Afterwards, the final images have been calculated by an algorithm that averages the images of both orientations. Tube setting have been 70 kV tube voltage and 100 mA tube current yielding a dose of 2.69 mGy measured as air kerma for the whole imaging procedure of the object measurement. If not mentioned otherwise, the dose for the presented images was reduced to 1.15 mGy (resepectively 231 mAs) including six of fourteen measurements, as the obtained image quality of this dose level is considered to be sufficient. Quantitative calculation has been carried out at various dose levels using 2 to 14 measurements. To broaden the range of examined dose levels to the lower end, additional reconstructions have been carried out with a reduced number of phase steps. Thereby, the lowest dose sums up to 0.14 mGy using only 4 of 11 phase steps of a single measurement for both orientations. We used a DC300 ionization chamber of IBA dosimetry to measure the dose.

Since the field of view is too small to measure the knee at once, the images are composed by a number of 91 tiles (respectively 98 tiles in the rotated orientation), each showing a crop of the final image. A new reference measurement was performed for every column of the tiling process to prevent phase drift effects due to mechanical instabilities of the setup. The complete measurement procedure took 4 h 26 min, respectively 1 h 54 min for the presented images. This rather long time is needed because of the tiling procedure which would not be necessary if a sufficient size of the gratings would be available.

2.4. Image processing

We corrected reference phase drift artifacts in the differential phase image with a method based on the approach in Kaeppler *et al* (2014). The method models the phase drift in each tile as polynomial images, which are weighted and subtracted from the measured differential phase images. The weights are determined such that the total variation of the resulting images is minimized, while also promoting smooth temporal changes of the weights.

As the scope of the reported measurement aims at medical imaging, we suggest a depiction of the image information of the differential phase-contrast information in a way that

overcomes the inherent differential image impression. A differential image impression impedes the interpretation of the image and is not familiar in clinical practice. A simple, straightforward line integration of the differential information is not feasible because the integration process amplifies low-frequency noise in the integrated image (Kottler *et al* 2007, Thüring *et al* 2011, Scherer *et al* 2014). Therefore, we suggest the following depiction of differential phase-contrast information instead of a straightforward integration. The method is equivalent to the Hilbert-filter-based visualization of differential images by Arnison *et al* (2000) in differential interference contrast microscopy.

Due to the integration property of the fourier transform the integration in space can be carried out as a multiplication in spatial frequency according to

$$\int_{-\infty}^{t} x(\tau)\mathrm{d}\tau = \mathcal{F}^{-1}\left(\frac{1}{\mathrm{i}k}\hat{X}(k)\right), \qquad \text{if} \qquad \hat{X}(0) = \int_{-\infty}^{\infty} x(\tau)\mathrm{d}\tau = 0 \tag{4}$$

is fulfilled with $\hat{X}$ being the Fourier transformed differential phase-contrast image. The one-dimensional operation was carried out in direction of the phase sensitivity for both orientations of the knee. For a medical image this is usually the case or can be assumed. The divison by k in Fourier space acts as a low-pass filter, which amplifies low frequency noise disturbing the image. Hence, only the division by i has been applied yielding a high-pass filtered phase image. We emphasize that solely the information of the differential phase-contrast image has been used and therefore the resulting image will be named high-frequency phase-contrast image in the following.

No filtering has been applied to the attenuation and dark-field image to keep the following calculation of contrast-to-noise ratios unaffected of image post-processing.

3. Results

We imaged the human knee in our Talbot–Lau setup and obtained the three image modalities presented in figure 3. Thereby, the phase-contrast image (in the middle) and the dark-field image (bottom) reveal several features that are additional or better visible in comparison to the conventional attenuation image (top) and will be discussed in the following. The structures are marked in the respective images.

The image based on the high-frequency phase-contrast image contains information about soft tissue structures that are not visible in the conventional attenuation image. These comprise the anterior horn of the medial meniscus, the posterior horn of the medial meniscus, and the posterior cruciate ligament, all depicted by a brighter gray value. A magnified image of the joint gap region of the knee is shown in figure 4. The aforementioned features have been marked by red arrows.

The dark-field image shows two conspicuous bright lines in the joint cavity at the place of the posterior horn of the medial meniscus. In a medical reading these lines have been identified as signs of chondrocalcinosis, which is also defined as calcium pyrophosphate dihydrate (CPPD) crystal deposition disease. Most cases are idiopathic, but some metabolic and endocrine disorders can promote the deposition of CPPD in the cartilage matrix.

In order to proof the diagnosis of chondrocalcinosis, the medial meniscus was extracted and a histological examination was performed using the von Kossa staining method. A decalcification was not applied to the extracted tissue before it was cut into sections to preserve the calcified tissue. A von Kossa-stained histological section is shown in figure 5. The left hand-side depicts an overview over the complete section. Thereby, the brown areas (rhombus) can easily be seen depicting calcified areas. On the right hand-side a magnification of the blue

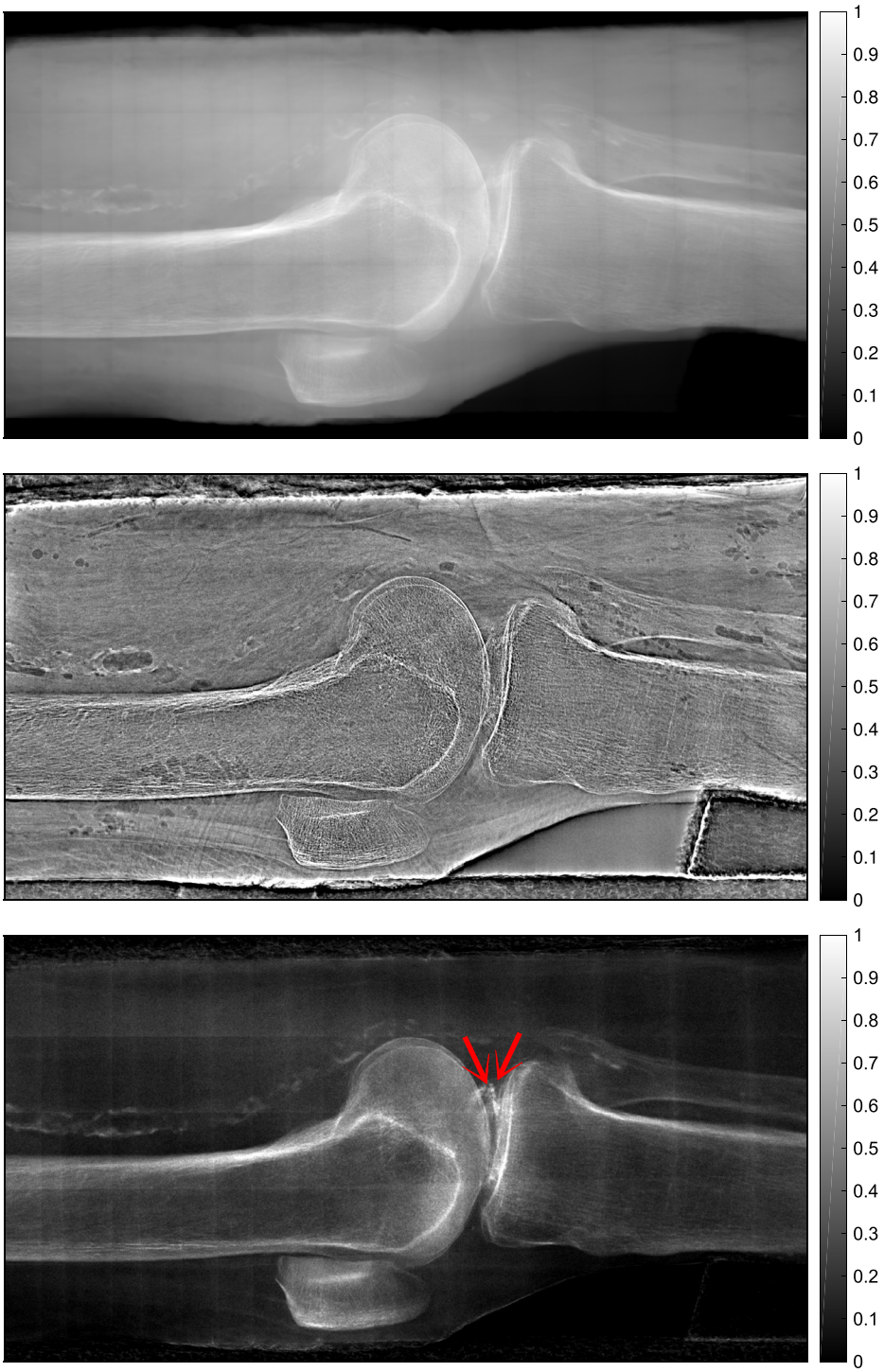

Figure 3. From top to bottom: attenuation, high-frequency phase-contrast and dark-field image of an *ex vivo* human knee measured at 70 kVp. In the dark-field image the red arrows point to signatures of chondrocalcinosis. The dose amounts to 1.15 mGy.

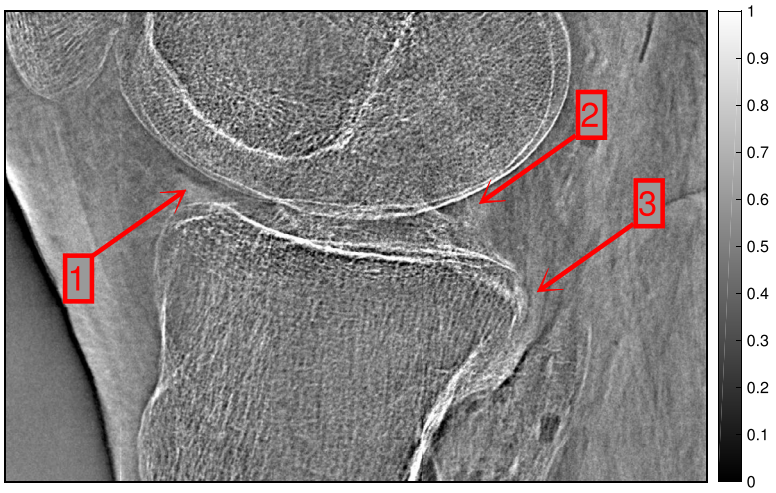

Figure 4. High-frequency phase-contrast image of the knee joint gap area. The image was rotated compared to figure 3 by 90°. Several soft tissue features are visible and indicated by the arrows. 1: anterior horn of the medial meniscus, 2: posterior horn of the medial meniscus, 3: posterior cruciate ligament.

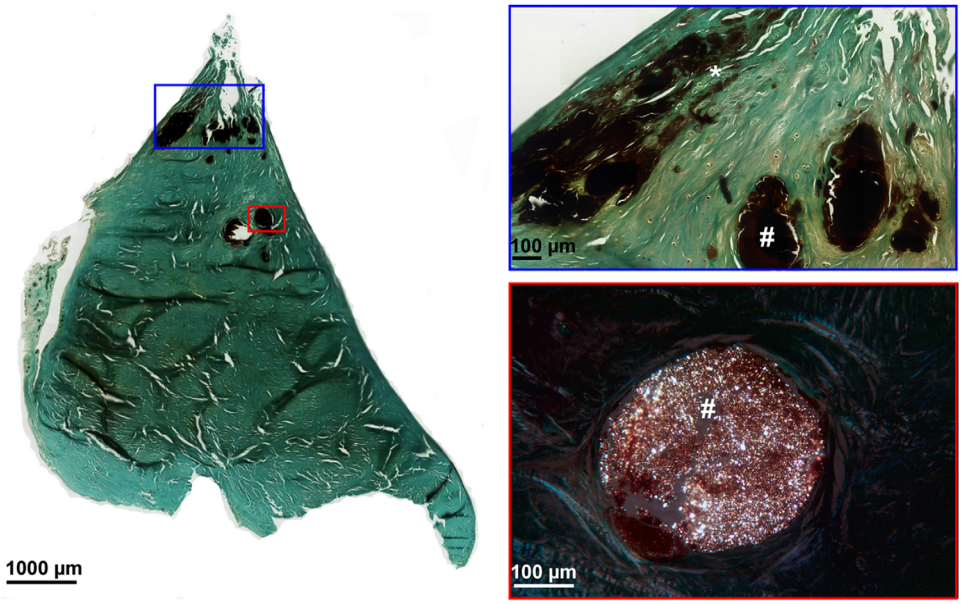

Figure 5. On the left-hand side: overview of the von Kossa-stained meniscus. Brown areas (rhombus) can be recognized depicting calcified areas. On the right-hand side: in the blue inset chondrometaplasia is visible (asterisk) around the calcified areas. The red inset depicts crystals revealed by polarization microscopy. The form and size of the crystals are typical for chondrocalcinosis.

inset is shown at the top. An asterisk marks the *chondrometaplasia* which is visible around the calcified areas. Below a magnified image of the red inset depicts crystals which light up due to birefringence in polarization microscopy. The form and shape of the crystals are typical for calcium pyrophosphate dihydrate deposited by chondrocalcinosis.

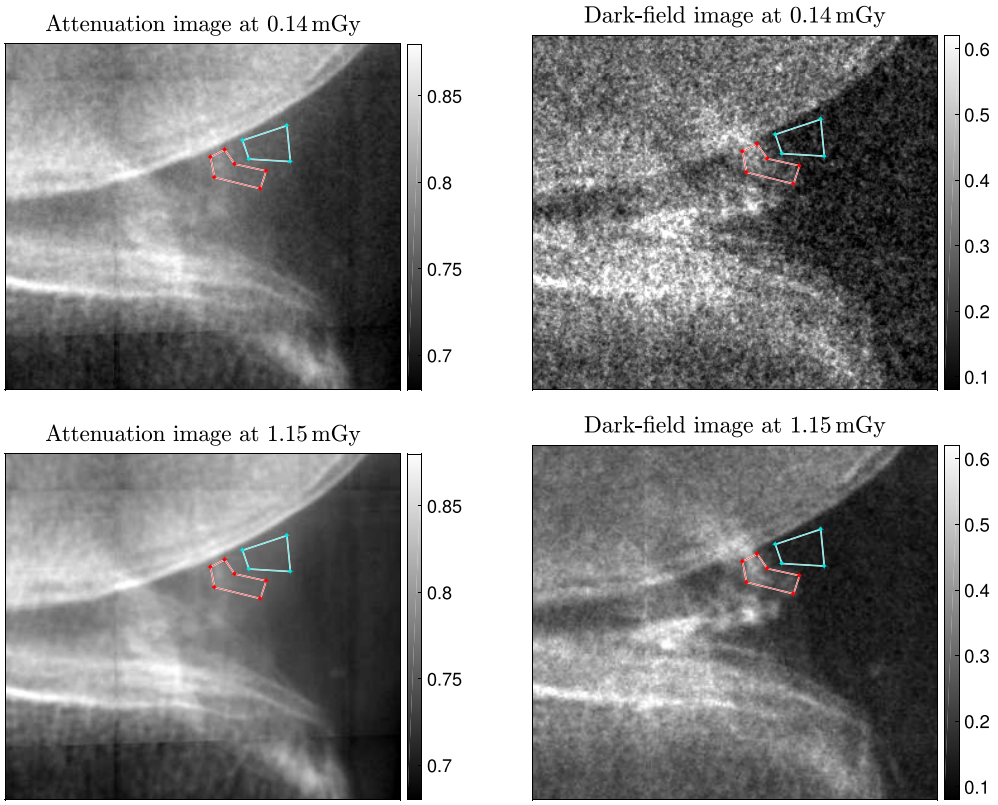

Figure 6. Detail images of the joint gap region of the knee for the attenuation and dark-field images. Comparing the upper and lower row, the dose increases from 0.14 mGy to 1.15 mGy showing a decrease in noise. The red line marks the signal ROI while the turquoise line marks the region for the calculation of the noise.

As chondrocalcinosis describes the deposition of highly absorbing CPPD crystals in cartilaginous tissue, it can be already diagnosed in the attenuation image. However, conventional radiography detects only about 40% of CPPD deposits (Miksanek and Rosenthal 2015). Provided the additional image modality of dark-field imaging, the possibility arises that Talbot–Lau imaging can forward the detectibility of chondrocalcinosis.

Therefore, contrast-to-noise ratio (CNR) determination has been carried out for the attenuation and dark-field image according to

$$\mathrm{CNR} = \frac{S_{\mathrm{signal}} - S_{\mathrm{background}}}{\sigma_{\mathrm{background}}} \tag{5}$$

with S_{signal} respectively $S_{\mathrm{background}}$ being the averaged gray values in the signal and background region of interest (ROI) and $\sigma_{\mathrm{background}}$ being the standard deviation in the background region. The signal ROI was excluded from the calculation of the image noise due to lacking homogeneity with regard to the underlying anatomical structure.

For the calculation a signal ROI was chosen that comprises a part of the affected meniscus tissue that is not overlayed by a bone. The chosen signal ROI and the background region for the calculation of the CNR is shown in figure 6 marked by a red line for the signal ROI and a turquoise line for the background ROI. The background was chosen to be close to the signal ROI not overlapping with a region containing bone.

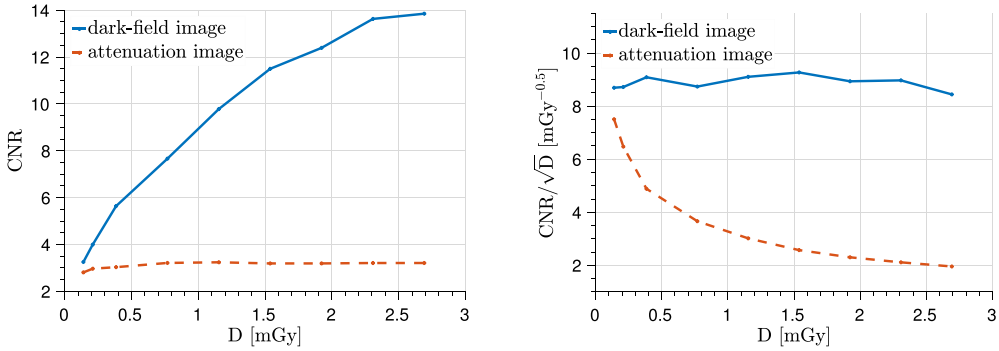

Figure 7. On the left-hand side: calculated CNRs for both dark-field and attenuation image over various dose levels. On the right-hand side: calculated CNR/$\sqrt{D}$ for both dark-field and attenuation image over various dose levels.

The figure contains the attenuation and the dark-field image for two different dose levels. The images of the upper row were calculated using an exposure of 0.14 mGy while the dose was raised to 1.15 mGy for the lower row. The increase in dose yields visibly lower noise, which is more evident for the dark-field image.

For a quantitative comparison the CNR has been calculated according to equation (5) and is plotted in figure 7. The obtained CNR of the dark-field image surpasses the attenuation image for all examined dose levels. Thereby, the upside of the dark-field image is larger the higher the dose D, as the CNR of the dark-field image keeps increasing while the CNR of the attenuation image is rather uneffected by an increase in dose. This is even more evident if the obtained CNR values are divided by the square root of the dose (CNR/$\sqrt{D}$), as shown on the right-hand side of figure 7. Since the contribution to the uncertainties in the attenuation and dark-field image by the detector quantum noise are inversely proportional to the square root of the dose

$$\frac{\sigma_\Gamma}{\Gamma} \propto \frac{1}{\sqrt{D}} \qquad \text{and} \qquad \frac{\sigma_\Sigma}{\Sigma} \propto \frac{1}{\sqrt{D}}, \tag{6}$$

as shown in Revol *et al* (2010), the CNR/$\sqrt{D}$ is expected to be independent of dose for both image modalities. For the dark-field image this behavior can be observed, whereas the value decreases in the attenuation image.

The occurrence of gray values in histograms of the signal ROI and background ROI for the attenuation and the dark-field image (see figure 8) provides the explanation. In the upper row the lowest possible dose of the measurement with 0.14 mGy was used. Please note that the gray values of the dark-field image are spread over a four times larger scale compared to the attenuation image. To account for the different spread the width of the bins has been adjusted accordingly. Hence, the number of bins displayed in figure 8 matches between both imaging modalities. Increasing the dose to 1.15 mGy the histogram of the obtained gray values of the dark-field background region narrows due to lower noise, as shown in the lower row of figure 8. For the attenuation image the gray values remain rather unchanged. Hence, the CNR does not increase due to lower σ_Γ. This can be explained by an already low noise level of the lowest examined dose. Consequently, the standard deviation of the gray values is dominated by anatomical inhomogeneity within the background region that surpasses the differences due to noise.

In addition, signs of severe atherosclerosis have been found in the popliteal artery, which are visible in both the attenuation and the dark-field image. Both imaging modalities are

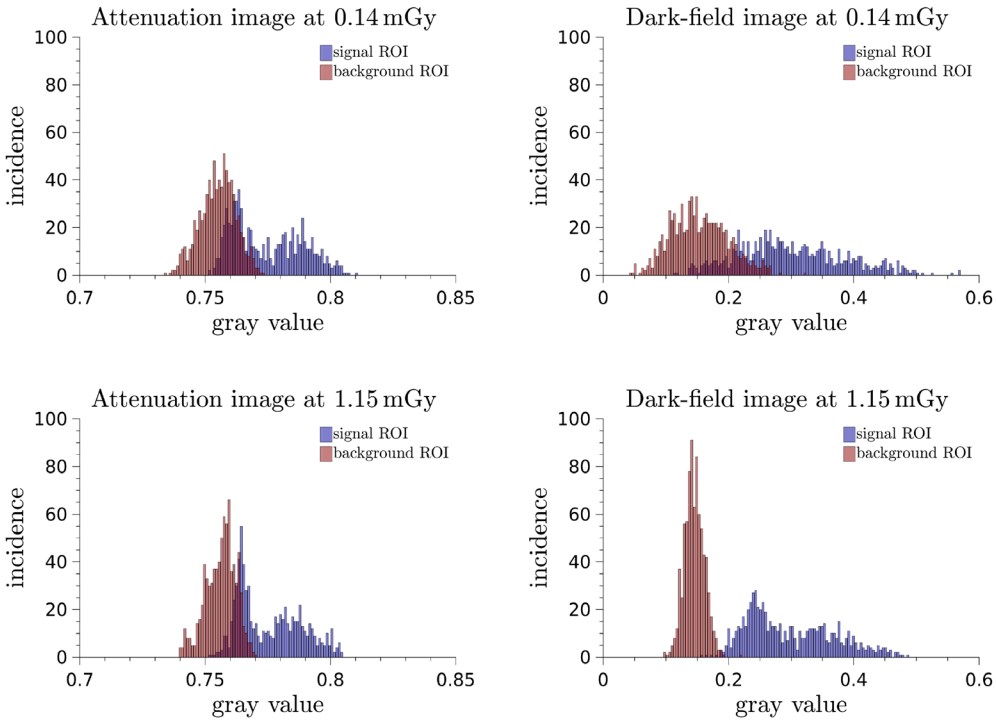

Figure 8. Occurrence of gray values of the signal ROI and the background ROI for both the attenuation and dark-field image. In the upper row the histograms for a dose of 0.14 mGy and in the lower row for 1.15 mGy are shown.

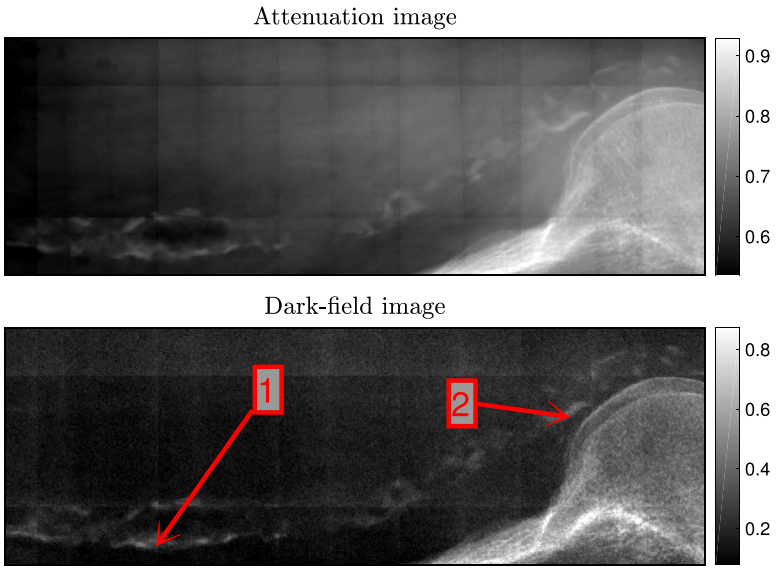

Figure 9. Attenuation (top) and dark-field image (bottom) of the popliteal artery containing atherosclerotic plaque that is visible in both image modalities. Red arrows 1 and 2: examples of atherosclerotic calcified plaque in the dark-field image.

shown in figure 9. To provide clarification, a bubble of air has been marked by the red arrow 1 in the attenuation image that was hold by the popliteal artery. In the dark-field image examples of calcified atherosclerotic plaque are marked by the red arrows 2 and 3.

The popliteal artery has been harvested and opened showing clear evidence of spatially extensive calcifications.

4. Discussion

The reported measurement is, to the best of our knowledge, unprecedented in literature regarding the thickness traversed and absorption of the x-rays by the object in grating-based phase-contrast imaging using a medical x-ray tube. In order to achieve sufficient flux the tube voltage has been set to 70 kV reaching an average visibility of 28%, which currently represents a high value. Thereby, the interferomter can be used reasonably for tube voltages between 45 kV and 125 kV appropriate for most parts of the human body.

There are several publications available that report on a similar or even higher maximum photon energy. But those either refer to measurements carried out at a synchrotron beam (Willner *et al* 2013, Ruiz-Yaniz *et al* 2015) or have been used for computed tomography images of smaller objects (Sarapata *et al* 2015).

A different approach has been pursued by Thüring *et al* (2014) employing gratings with edge-on illumination. Using this technique the necessary grating-heights for high-energy medical imaging (and beyond) can be reached, but the small field of view entails the need to scan the object and impedes grating alignment. The dimensions of the setup have been restricted, too.

The different imaging modalities of Talbot–Lau imaging revealed several noticeable features. The high-frequency phase-contrast image provided soft tissue contrast regarding the anterior and posterior horn of the medial meniscus as well as the posterior cruciate ligament. These structures are commonly not distinguishable by conventional radiography and usually require magnetic resonance imaging entailing high demands with regard to cost and time.

Further, signs of chondrocalcinosis of the meniscus tissue have been found in the dark-field image. This finding was confirmed by a histological examination that revealed the presence of CPPD crystals within the lesions. A quantitative analysis with the contrast-to-noise ratio as criterion yielded higher values for the dark-field image at all studied dose levels. Thereby, the lowest examined dose of 0.14 mGy, measured as air kerma, is comparable to clinically used radiographic devices (Huda and Gkanatsios 1998, Kwang *et al* 2009). However, the used setup is still limited by the size of the G2 grating, which causes long acquisition times due to the necessary tiling procedure for large specimens. Future improvements regarding the interferometer setup and grating height of the absorbing source and analyzer gratings will forward the application of dark-field imaging. This respresents a great advantage compared to convential radiography, which suffers from a low sensitivity for depicting CPPD deposits (Miksanek and Rosenthal 2015).

Chondrocalcinosis has already been detetced in the human knee joint gap using diffraction-enhanced synchrotron imaging (Li *et al* 2013). With the translation from a synchrotron facility to grating-based phase-contrast using a medical x-ray tube the scatter-based depiction of CPPD deposits comes closer to application in the clinics.

Both, a more sensitive detection of calcium crystal deposits and the visualisation of soft tissue structures may also be of high clinical value for the diagnosis of chronic shoulder pain (Kachewar and Kulkarni 2013, ElShewy 2016). According to Nörenberg *et al* (2016) even standard rotator cuff magnetic resoncance sequences struggle in respect of sensitivity and

specificity. Future studies will investigate if the novel imaging technique is able to visualize lesions and calcium deposits within the rotator cuff in case of *tendinitis calcarea* of the shoulder.

The imaging of atherosclerosis has already drawn interest with regard to phase-contrast computed tomography (PC-CT) of harvested coronary arteries (Saam *et al* 2013, Hetterich *et al* 2015). Thereby, measurements using a synchrotron and a conventional medical x-ray tube have been carried out. It was proven that grating-based phase-contrast imaging is feasible for both setups showing enhanced soft tissue contrast that allows for the differentiation of vessel dimensions. The dose has been high with up to 18 Gy using a convential x-ray tube, though.

As microcalcifications have been identified to indicate higher risk of plaque rupture with the consequence of possible sudden stroke or myocardinal infarction (Hutcheson *et al* 2016), the dark-field image with its sensitivity towards microcalcifications is of major interest. We showed that the calcifications are visible in both the attenuation and dark-field image of a radiography measurement at a dose level within the reach of medical imaging. The plaque remains visible in the dark-field image despite the presence of overlaying bone of the fibula, as shown in figure 3. However, the process of calcification in the examined knee has been already advanced and the calcified plaque was found to be spatially large and solid. No signs of plaque that is visible only in the dark-field image without any manifestation in the attenuation image could be observed. Nonetheless, regarding atherosclerosis the dark-field imaging should be part of future research, since microcalcifications as a possible tumor marker have been ascertained, which are invisible concerning the attenuation image (Michel *et al* 2013).

In the phase-contrast image we could not observe any subtle soft-tissue details to identify uncalcified atherosclerotic plaque at the dose level of the measurement of 1.15 mGy. This may be due to the presence of highly absorbing calcifications, overlaying soft-tissue from the radiography image, and the high noise level as consequence of the low dose.

5. Conclusion

The measurement in its entirety shows the feasibility of Talbot–Lau imaging using a medical x-ray tube at high energies above 40 kVp and reasonable dose levels with regard to spacious and dense objects. Several features have been revealed in the resulting high-frequency phase-contrast and dark-field images which stand out against the attenuation image. Regarding the reported case of chondrocalcinosis it was shown that the dark-field yields a higher contrast-to-noise ratio than the attenuation image. In summary, the reported measurement represents an important landmark on the way of grating-based phase-contrast imaging towards the clinics.

Acknowledgments

This work was carried out with the support of the Karlsruhe Nano Micro Facility (KNMF), a Helmholtz Research Infrastructure at Karlsruhe Institute of Technology (KIT).

We would like to acknowledge financial and technical support of this work by Siemens Healthcare GmbH.

In addition, we acknowledge the contribution of Thorsten Hummel and Lisa Stache of the Anatomical Institute of the University of Erlangen who extracted the meniscus tissue and popliteal artery, as well as the contribution of Anita Hecht and Stefanie Link who cut the histological slices.

References

Arfelli F *et al* 2000 Mammography with synchrotron radiation: phase-detection techniques *Radiology* **215** 286–93

Arnison M R, Cogswell C J, Smith N I, Fekete P W and Larkin K G 2000 Using the hilbert transform for 3d visualization of differential interference contrast microscope images *J. Microsc.* **199** 79–84

Bayer F, Zabler S, Brendel C, Pelzer G, Rieger J, Ritter A, Weber T, Michel T and Anton G 2013 Projection angle dependence in grating-based x-ray dark-field imaging of ordered structures *Opt. Express* **21** 19922–33

Bech M, Tapfer A, Velroyen A, Yaroshenko B, Pauwels B, Hostens J, Bruyndonckx P, Sasov A and Pfeiffer F 2013 *In vivo* dark-field and phase-contrast x-ray imaging *Sci. Rep.* **3** 3209

Chapman D *et al* 1997 Diffraction enhanced x-ray imaging *Phys. Med. Biol.* **42** 2015–25

Chen G H, Zambelli J, Li K, Bevins N and Qi Z 2011 Scaling law for noise variance and spatial resolution in differential phase contrast computed tomography *Med. Phys.* **38** 584

Donath T, Pfeiffer F, Bunk O, Groot W, Bednarzik M, Grünzweig C, Hempel E, Popescu S, Hoheisel M and David C 2009 Phase-contrast imaging and tomography at 60 KeV using a conventional x-ray tube source *Rev. Sci. Instrum.* **80** 053701

ElShewy M T 2016 Calcific tendinitis of the rotator cuff *World J. Orthopedics* **7** 55–60

Engelhardt M, Baumann J, Schuster M, Kottler C, Pfeiffer F, Bunk O and David C 2007 High-resolution differential phase contrast imaging using a magnifying projection geometry with a microfocus x-ray source *Appl. Phys. Lett.* **90** 224101

Fitzgerald R 2000 Phase-sensitive x-ray imaging *Phys. Today* **53** 23–6

Hellbach K *et al* 2015 *In vivo* dark-field radiography for early diagnosis and staging of pulmonary emphysema *Invest. Radiol.* **50** 1–7

Hetterich H *et al* 2015 X-ray phase-contrast computed tomography of human coronary arteries *Invest. Radiol.* **50** 686–94

Huda W and Gkanatsios N 1998 Radiation dosimetry for extremity radiographs *Health Phys.* **75** 492–9

Hutcheson J D *et al* 2016 Genesis and growth of extracellular-vesicle-derived microcalcification in atherosclerotic plaques *Nat. Mater.* **15** 335–43

Jensen T H, Bech M, Bunk O, Donath T, David C, Feidenhans'l R and Pfeiffer F 2010 Directional x-ray dark-field imaging *Phys. Med. Biol.* **55** 3317–23

Kachewar S G and Kulkarni D S 2013 Calcific tendinitis of the rotator cuff: a review *J. Clin. Diagn. Res.* **7** 1482–5

Kaeppler S, Wandner J, Weber T, Maier A, Anton G, Hornegger J and Riess C 2014 Shading correction for grating-based differential phase contrast x-ray imaging *2014 IEEE Nuclear Science Symp. and Medical Imaging Conf.* (https://doi.org/10.1109/NSSMIC.2014.7430896)

Koenig T, Zuber M, Trimborn B, Farago T, Meyer P, Kunka D, Albrecht F, Kreuer S, Volk T and Fiederle M 2016 On the origin and nature of the grating interferometric dark-field contrast obtained with low-brilliance x-ray sources *Phys. Med. Biol.* **61** 3427

Kottler C, David C, Pfeiffer F and Bunk O 2007 A two-directional approach for grating based differential phase contrast imaging using hard x-rays *Opt. Express* **15** 1175–81

Kwang H L, Jong W K, Young C Y, Choi S H, Jee Y J, Ji H K and Sang J L 2009 Slot-scan digital radiography of the lower extremities: a comparison to computed radiography with respect to image quality and radiation dose *Korean J. Radiol.* **10** 51–7

Li J, Wilson N, Zelazny A, Meyer J, Zhong Z and Muehleman C 2013 Assessment of diffraction-enhanced synchrotron imaging for cartilage degeneration of the human knee joint *Clin. Anat.* **26** 621–9

Meyer P and Schulz J 2015 *Deep X-ray LIGA, Micromanufacturing Engineering and Technology* 2nd edn (Boston, MA: William Andrew Publishing) ch 16

Meyer P *et al* 2015 Deep x-ray lithography fabrication of x-ray gratings for grating based interferometry: a review *3rd Meeting of X-Ray and Neutron Phase Imaging with Gratings (XNPIG) (Bethesda, Maryland, USA, 8–11 September 2015)*

Michel T *et al* 2013 On a dark-field signal generated by micrometer-sized calcifications in phase-contrast mammography *Phys. Med. Biol.* **58** 2713–32

Miksanek J and Rosenthal A K 2015 Imaging of calcium pyrophosphate deposition disease *Curr. Rheumatol. Rep.* **17** 20

Momose A 2005 Recent advances in x-ray phase imaging *Japan J. Appl. Phys.* **44** 6355–67

Momose A, Kawamoto S, Koyama I, Hamaishi Y, Takai K and Suzuki Y 2003 Demonstration of x-ray Talbot interferometry *Japan J. Appl. Phys.* **52** L866–8

Momose A, Takeda T, Itai Y and Hirano K 1996 Phase contrast x-ray computed tomography for observing biological soft tissues *Nat. Med.* **2** 473–5
Momose A *et al* 2014 X-ray phase imaging: from synchrotron to hospital *Phil. Trans. R. Soc.* A **372** 20130023
Nagashima M, Tanaka J, Kiyohara J, Makifuchi C, Kido K and Momose A 2014 Application of x-ray grating interferometry for the imaging of joint structures *Anatomical Sci. Int.* **89** 95–100
Nörenberg D, Ebersberger H U, Walter T, Ockert B, Knobloch G, Diederichs G, Hamm B and Makowski M R 2016 Diagnosis of calcific tendonitis of the rotator cuff by using susceptibility-weighted mr imaging *Radiology* **278** 475–84
Olivo A *et al* 2001 An innovative digital imaging set-up allowing a low-dose approach to phase contrast applications in the medical field *Med. Phys.* **28** 1610–9
Olivo A *et al* 2007 A coded-aperture technique allowing x-ray phase contrast imaging with conventional sources *Appl. Phys. Lett.* **91** 074106
Parham C, Zhong Z, Connor D M, Chapman L D and Pisano E D 2009 Design and implementation of a compact low-dose diffraction enhanced medical imaging system *Acad. Radiol.* **16** 911–7
Pfeiffer F, Bech M, Bunk O, Kraft P, Eikenberry E F, Brönnimann C, Grünzweig C and David C 2008 Hard-x-ray dark-field imaging using a grating interferometer *Nat. Mater.* **7** 134–7
Pfeiffer F, Weitkamp T, Bunk O and David C 2006 Phase retrieval and differential phase-contrast imaging with low-brilliance x-ray sources *Nat. Phys.* **2** 258–61
Prade F, Fischer K, Heinz D, Meyer P, Mohr J and Pfeiffer F 2016 Time resolved x-ray dark-field tomography revealing water transport in a fresh cement sample *Sci. Rep.* **6** 29108
Revol V, Kottler C, Kaufmann R, Neels A and Dommann A 2012 Orientation-selective x-ray dark field imaging of ordered systems *J. Appl. Phys.* **112** 6
Revol V, Kottler C, Kaufmann R, Straumann U and Urban C 2010 Noise analysis of grating-based x-ray differential phase contrast imaging *Rev. Sci. Instrum.* **81** 073709
Rieger J, Meyer P, Horn F, Pelzer G, Michel T, Mohr J and Anton G 2017 Optimization procedure for a Talbot-Lau x-ray phase-contrast imaging system *J. Instrum.* **12** P04018
Rieger J, Meyer P, Pelzer G, Weber T, Michel T, Mohr J and Anton G 2016 Designing the phase grating for Talbot-Lau phase-contrast imaging systems: a simulation and experiment study *Opt. Express* **24** 13357–64
Ruiz-Yaniz M, Koch F, Zanette I, Rack A, Meyer P, Kunka D, Hipp A, Mohr J and Pfeiffer F 2015 X-ray grating interferometry at photon energies over 180 KeV *Appl. Phys. Lett.* **106** 151105
Saam T *et al* 2013 Translation of atherosclerotic plaque phase-contrast ct imaging from synchrotron radiation to a conventional lab-based x-ray source *PLoS ONE* **8** e73513
Sarapata A *et al* 2015 Quantitative imaging using high-energy x-ray phase-contrast ct with a 70 kvp polychromatic x-ray spectrum *Opt. Express* **23** 523–35
Schaff F, Malecki A, Potdevin G, Eggl E, Noël P B, Baum T, Garcia E G, Bauer J S and Pfeiffer F 2014 Correlation of x-ray vector radiography to bone micro-architecture *Sci. Rep.* **4** 3695
Scherer K, Birnbacher L, Chabior M, Herzen J, Mayr D, Grandl S, Sztrókay-Gaul A, Hellerhoff K, Bamberg F and Pfeiffer F 2014 Bi-directional x-ray phase-contrast mammography *PloS One* **9** e93502
Scherer K *et al* 2016 Improved diagnostics by assessing the micromorphology of breast calcifications via x-ray dark-field radiography *Sci. Rep.* **6** 36991
Stampanoni M, Wang Z, Thring T, David C, Roessl E, Trippel M, Kubik-Huch R A, Singer G, Hohl M K and Hauser N 2011 The first analysis and clinical evaluation of native breast tissue using differential phase-contrast mammography *Invest. Radiol.* **46** 801–6
Thüring T, Abis M, Wang Z, David C and Stampanoni M 2014 X-ray phase-contrast imaging at 100 keV on a conventional source *Sci. Rep.* **4** 5198
Thüring T, Modregger P, Hammerle S, Weiss S, Nuesch J and Stampanoni M 2011 Non-linear regularized phase retrieval for unidirectional x-ray differential phase contrast radiography *Opt. Express* **19** 25545
Trimborn B, Meyer P, Kunka D, Zuber M, Albrecht F, Kreuer S, Volk T, Baumbach T and Koenig T 2016 Imaging properties of high aspect ratio absorption gratings for use in preclinical x-ray grating interferometry *Phys. Med. Biol.* **61** 527
Velroyen A *et al* 2015 *Ex vivo* perfusion-simulation measurements of microbubbles as a scattering contrast agent for grating-based x-ray dark-field imaging *PLoS One* **10** 1–4

Weber T, Bartl P, Bayer F, Haas W, Michel T, Ritter A and Anton G 2011 Noise in x-ray grating-based phase-contrast imaging *Med. Phys.* **38** 4133–40
Weitkamp T, Diaz A, David C, Pfeiffer F, Stampanoni M, Cloetens P and Ziegler E 2005 X-ray phase imaging with a grating interferometer *Opt. Express* **13** 6296–304
Willner M, Bech M, Herzen J, Zanette I, Hahn D, Kenntner J, Mohr J, Rack A, Weitkamp T and Pfeiffer F 2013 Quantitative x-ray phase-contrast computed tomography at 82 KeV *Opt. Express* **21** 4155
Yaroshenko A *et al* 2014 Grating-based x-ray dark-field imaging: a new paradigm in radiography *Curr. Radiol. Rep.* **2** 57
Yaroshenko A *et al* 2016 Visualization of neonatal lung injury associated with mechanical ventilation using x-ray dark-field radiography *Sci. Rep.* **6** 24269
Yashiro W, Terui Y, Kawabata K and Momose A 2010 On the origin of visibility contrast in x-ray Talbot interferometry *Opt. Express* **18** 16890–901